Remote Sens. **2015**, *7*, 14530-14558; doi:10.3390/rs71114530

OPEN ACCESS

remote sensing

ISSN 2072-4292

www.mdpi.com/journal/remotesensing

Article

Spatiotemporal Variation in Mangrove Chlorophyll Concentration Using Landsat 8

Julio Pastor-Guzman [1], Peter M. Atkinson [1,2,3,4,†], Jadunandan Dash [1,*] and Rodolfo Rioja-Nieto [5]

[1] Global Environmental Change and Earth Observation Research Group, Geography and Environment, University of Southampton, Southampton SO17 1BJ, UK; E-Mails: J.Pastor-Guzman@soton.ac.uk (J.P.-G.); pma@lancaster.ac.uk (P.M.A.)

[2] Faculty of Science and Technology, Lancaster University, Lancaster LA1 4YR, UK

[3] Faculty of Geosciences, University of Utrecht, Heidelberglaan 2, Utrecht CS 3584, The Netherlands

[4] School of Geography, Archaeology and Palaeoecology, Queen's University Belfast, Belfast BT7 1NN, Northern Ireland, UK

[5] Academic Unit Sisal, Faculty of Sciences, National Autonomous University of Mexico, Sisal, Yucatan 97355, Mexico; E-Mail: rrioja@ciencias.unam.mx

† The author contributed equally to this work.

* Author to whom correspondence should be addressed; E-Mail: J.DASH@soton.ac.uk; Tel.: +23-8059-7347.

Academic Editors: Chandra Giri, Clement Atzberger and Prasad S. Thenkabail

Received: 29 August 2015 / Accepted: 26 October 2015 / Published: 4 November 2015

Abstract: There is a need to develop indicators of mangrove condition using remotely sensed data. However, remote estimation of leaf and canopy biochemical properties and vegetation condition remains challenging. In this paper, we (i) tested the performance of selected hyperspectral and broad band indices to predict chlorophyll concentration (CC) on mangrove leaves and (ii) showed the potential of Landsat 8 for estimation of mangrove CC at the landscape level. Relative leaf CC and leaf spectral response were measured at 12 Elementary Sampling Units (ESU) distributed along the northwest coast of the Yucatan Peninsula, Mexico. Linear regression models and coefficients of determination were computed to measure the association between CC and spectral response. At leaf level, the narrow band indices with the largest correlation with CC were Vogelmann indices and the MTCI ($R^2 > 0.5$). Indices with spectral bands around the red edge (705–753 nm) were more

sensitive to mangrove leaf CC. At the ESU level Landsat 8 NDVI green, which uses the green band in its formulation explained most of the variation in CC ($R^2 > 0.8$). Accuracy assessment between estimated CC and observed CC using the leave-one-out cross-validation (LOOCV) method yielded a root mean squared error (RMSE) = 15 $\mu g \cdot cm^{-2}$, and $R^2 = 0.703$. CC maps showing the spatiotemporal variation of CC at landscape scale were created using the linear model. Our results indicate that Landsat 8 NDVI green can be employed to estimate CC in large mangrove areas where ground networks cannot be applied, and mapping techniques based on satellite data, are necessary. Furthermore, using upcoming technologies that will include two bands around the red edge such as Sentinel 2 will improve mangrove monitoring at higher spatial and temporal resolutions.

Keywords: Landsat 8; mangrove; spatiotemporal; chlorophyll map; vegetation indices

1. Introduction

Mangrove forests cover approximately 13.7 million ha of tropical and subtropical shorelines across 118 countries [1]. Worldwide, Mexico ranks fourth in terms of mangrove coverage (742,000 ha), with 55% of the coverage distributed along the coast of the Yucatan Peninsula. Mangrove forests provide a wealth of direct and indirect ecosystem services such as natural protection barriers and nursery habitat for marine organisms [2–5]. Further, the ability of mangrove forests to act as a carbon (C) sink has been the focus of recent research. Estimates suggest that mangrove C storage ranges between ~160 $Mg \cdot ha^{-1}$ and ~1000 $Mg \cdot ha^{-1}$ depending on location, species composition, height, and canopy closure [6,7]. Data on C stocks have been published for numerous mangrove systems across the globe including Australia [6], China [8], Indo-Pacific [7,9], Western-Pacific [10], Caribbean [11], and Mexico [12]. In addition, C removal from the atmosphere has been estimated at around 1,170 ± 127 $g \cdot C \cdot m^{-2} \cdot year^{-1}$ [13]. These figures acquire relevance in the context of climate change mitigation as C sequestration is emerging as a major strategy to reduce atmospheric C. In spite of the array of ecosystem services provided by mangroves, their high productivity, and their role played in C dynamics at the land–ocean interface [14], large areal losses are presently occurring due to deforestation and land use conversion due to both human and natural drivers [15,16].

The high productivity and C uptake of mangroves are intimately linked to photosynthesis, which is largely dependent on the availability of leaf pigments. Chlorophylls (Chl) are the most important leaf pigments responsible for photosynthesis. Leaf pigments have been identified as indicators of physiological status, senescence and stress [17,18]. This is also true in mangroves, which exhibit pigment variation between species and health conditions [19–21]. Furthermore, mangroves are subject to a range of environmental gradients that vary seasonally, potentially inducing stress. In a coastal lagoon system that was markedly seasonal in terms of water availability, Flores-de-Santiago Kovacs and Flores-Verdugo [21,22] found higher Chl *a* concentration during the rainy season in two species of degraded dwarf stands, suggesting that precipitation patterns might have an effect on leaf biochemical constituents and possibly on the total productivity of the mangrove forest.

Given the potential of Chl to act as a surrogate of vegetation status, Chl has become a key biophysical variable to monitor. The standard approach to estimating Chl concentration (CC) involves extracting the leaf pigment using an organic solvent followed by spectrophotometric determination of absorbance in the laboratory and, finally, conversion to CC using empirical equations [23,24]. A more practical technique that complements the aforementioned approach consists on the use of portable Chl meters such as the Opti-Sciences CCM-200 Chlorophyll Content Meter (CCM-200) and Minolta SPAD-502 Chlorophyll Meter (SPAD-502). Portable Chl meters have been used extensively in precision agriculture and have been tested on a variety of tree species [25–29]. To our knowledge, the first documented example of the use a portable Chl meter in mangrove species is Connelly [30]. Connelly [30] reported a large correlation between CC and Minolta SPAD-502 readings in red mangrove (*Rhizophora mangle*) ($R^2 > 0.6$ total Chl; $R^2 > 0.7$ Chl *a*). Years later, Biber [31] assessed the CCM-200 in *R. mangle* ($R^2 > 0.9$ Chl *a*) and other wetland species. Recently, Flores-de-Santiago Kovacs and Flores-Verdugo [32] documented large correlations for healthy stands of three mangrove species (*R. mangle* $R^2 > 0.76$, *Laguncularia racemosa* $R^2 > 0.68$ and *Avicennia germinans* $R^2 > 0.74$; rainy season) using the CCM-200. Calibration equations need to be applied to use portable Chl meter readings to convert these readings to actual chlorophyll concentration.

Remote sensing offers an alternative set of techniques to estimate chlorophyll concentration. These can be grouped into two main categories: (i) Radiative transfer models and (ii) vegetation indices (VIs). The physically based canopy reflectance model relies on the principle that canopy reflectance is controlled by a combination of canopy and soil background biophysical variables such as vegetation structure, leaf composition, and illumination angle [33–35]. To estimate Chl from observed reflectance data, the physical model must be inverted. The inversion consists of adjusting the input biophysical variables to reduce the error between the simulated and measured reflectance [36,37]. While these techniques have been applied with success [38,39], they can be computationally demanding. In addition, they suffer from the so-called ill-posed problem [40,41] due to model and measurements uncertainties; that is, different model parameters might result in very similar spectra [42]. The VI approach is based on the statistical or empirical relationship between arithmetic combinations of two or more spectral bands and a particular leaf or canopy characteristic (*i.e.*, chlorophyll concentration) [43]. It has been argued that this approach is sensor-specific, site-dependent, and does not account for variability in LAI. However, the VI approach offers computational simplicity and accuracy, and its potential for predicting vegetation variables is well supported by numerous published studies [40,44].

VIs can be derived from hyperspectral and multispectral data. Several studies have examined the relationship of VIs and CC leaf hyperspectral response at the leaf level [19,41,45]. Sensors on board different satellites have estimated vegetation CC using VIs at varying spatial resolutions, from a few to hundreds of meters [46–48]. While field spectroscopy and satellite-derived VIs have been used to estimate the chlorophyll content in leaves and canopies in different vegetation types, only few studies have focused on mangrove forests [21,22,30,32]. The spatial distribution and seasonal dynamics of mangrove forest CC is not well understood as previous studies have been spatially localized. Given the importance of foliar pigments as surrogates of mangrove physiological status, phenology, health condition, and potentially GPP, it is fundamental to assess the accuracy of VIs to predict CC at the leaf and landscape level. Our main goal is to show for the first time that the multispectral sensor Landsat 8 can be potentially used to produce maps of spatial distribution and temporal variation of chlorophyll concentration in mangrove forests.

The objectives of this research were to (a) assess the performance of selected hyperspectral and broad band VIs for predicting CC at the leaf level, and (b) relate the estimated CC on the ground with Landsat 8 data to map the spatial distribution and temporal variability of mangrove CC at the landscape level.

2. Methods

2.1. Study Area

The NW of the Yucatán Peninsula is characterized by a semi-arid climate [49] with three clear, distinct seasons: A dry season from March to May, a rainy season from June to October, and a third season characterized by cold fronts locally known as "Nortes" from November to February [50]. Topographic features on land do not exceed 2 m elevation, and the mangrove forest extends parallel to the coast [51] (Figure 1). Two protected areas are established in the region, El Palmar State Reserve and the Biosphere Reserve of Ría Celestún. Mangrove communities in the protected areas are well developed with four species dominating the landscape: *R. mangle*, *L. racemosa*, *A. germinans*, and *Conocarpus erectus*. The karstic nature of the ground favors the rapid infiltration of rainfall, resulting in the absence of runoff and the lack of important streams above the surface. Furthermore, wetland and floodplain flooding is controlled by groundwater discharge. In the wet season, aquifers recharge and reach saturation. At this point the water displaces horizontally while a fraction of it is discharged through sinkholes and fractures known locally as "petenes" Surface water is reduced significantly in the dry season, confined to pools and saturated soils adjacent to the sinkholes [51].

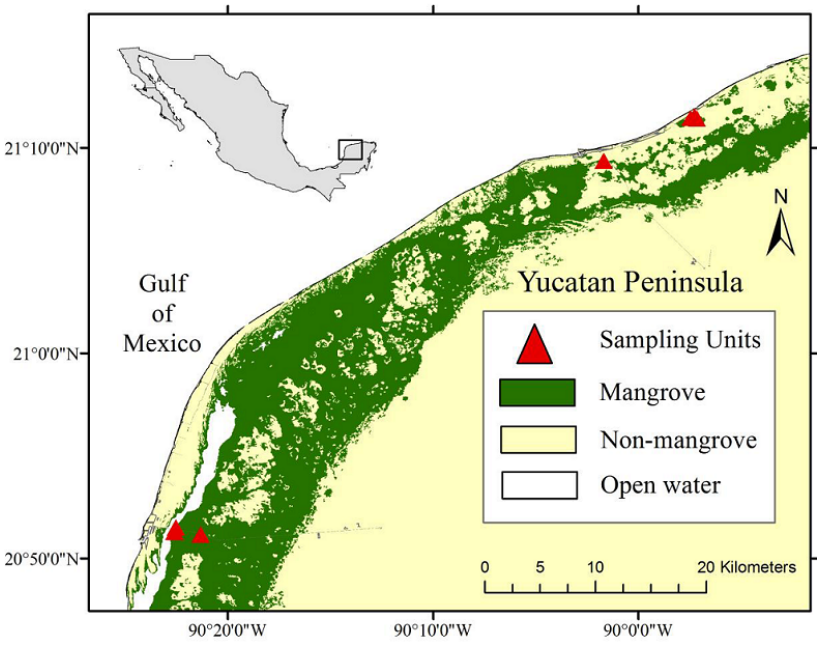

Figure 1. Location of sampling units in the mangrove forest in the north west of Yucatan peninsula.

Based on tidal patterns and surface drainage (geomorphology and hydrology), Lugo and Snedaker [52] proposed a classification scheme for mangrove forest. According to their framework, six well-defined physiognomic types are distinguishable: fringe, riverine, overwashed, basin, scrub, and hammock.

Except for the riverine type, all forest types are found in the NW of Yucatan Peninsula. In the study area, four types have been recognized: fringe, dwarf, basin, and peten [53]. Fringe mangroves occur along the edge of the lagoon, composed mainly by *R. mangle* at the front and *L. racemosa* at the interior zone. Fringe mangroves reach 12–14 m in height and are exposed to daily tidal inundation [54]. On the contrary, dwarf mangroves develop in highly saline environments with limited nutrient input and generally they do not exceed 4 m; dwarf mangroves are composed mainly by R. mangle, followed by *A. germinans* and *L. racemosa* [52,54,55]. Basin mangroves distribute inland, north of the study area, along drainage depressions. They are flooded by runoff and the dominant species are *A. germinans* and *R. mangle* [54]. Peten mangroves, also known as "hammocks" consist of characteristic islands of vegetation that stand out from a surrounding matrix composed of dwarf mangrove and savannah. These islands may reach 20–25 m and flourish over freshwater springs. Therefore, salinity is considerably lower and nutrient input is constant [54]. Representative species of this type of mangrove include *R. mangle*, *A. germinans*, and *L. racemosa*, associated with other evergreen and semi-evergreen tropical trees intolerant to salinity [54,56].

2.2. Data Acquisition

A field campaign was carried out between 7 and 14 January 2014. The purpose of the fieldwork was to collect leaf hyperspectral data and SPAD-Chlorophyll meter readings. Multispectral Landsat 8 data were acquired on 28 January to measure the association between CC and satellite-derived VIs. Landsat 8 was selected in this study given that its medium spatial resolution (30 m) enables capture of the heterogeneity of the mangrove landscape while its spectral resolution enables the computation of broad band indices highly correlated with CC [1,57]. In addition, Landsat 8 is the most recent instrument of the Landsat mission and has a similar spatial resolution to the future Sentinel 2 MSI sensor; therefore, it allows the continuity of mangrove chlorophyll concentration monitoring.

The leave-one-out cross-validation (LOOCV) method was used to validate the relationship between CC at the ESU level and Landsat 8 NDVI green. Figure 2 provides a schematic overview of the methodology followed in this paper.

Ground Data Collection

Twelve elementary sampling units (ESUs) of 30 m by 30 m to represent the Landsat spatial resolution were sampled. Coordinates were recorded at each ESU with a Global Positioning System (GPS) handheld receiver unit e-Trex (GARMIN International, Inc), with <15 m accuracy. At the center of each ESU two or three trees were sampled, according to species richness. To take account of the uneven distribution of CC in the canopy [58], on each sampled tree 15 leaves were taken from the top of the canopy and 15 leaves from below the top. The following measurements were performed for each tree:

(i) Leaf hyperspectral measurements: Leaf adaxial spectra were measured using the leaf clip of the Analytical Spectral Devices (ASD) Field Spec Pro spectrometer (Analytical Spectral Devices, Boulder, CO, USA) with a 350–2500 nm spectral range. Three scans were taken per leaf. The ASD spectrum averaging per scan was set to 25. Optimization and dark current collection were performed before measuring each leaf.

(ii) Leaf Chlorophyll: All leaves used in (i) were measured using a portable Minolta SPAD-502 Chlorophyll Meter (SPAD-502). The average of five SPAD readings evenly distributed around the leaf adaxial face was taken to represent the CC. Calibration equations were used to convert the SPAD values to actual chlorophyll concentration. Finally, the ESU CC was expressed as the average of the total number of leaves measured per ESU. For example, if in one ESU the total number of leaves measured were 90, the chlorophyll concentration would be the average of 90 leaves.

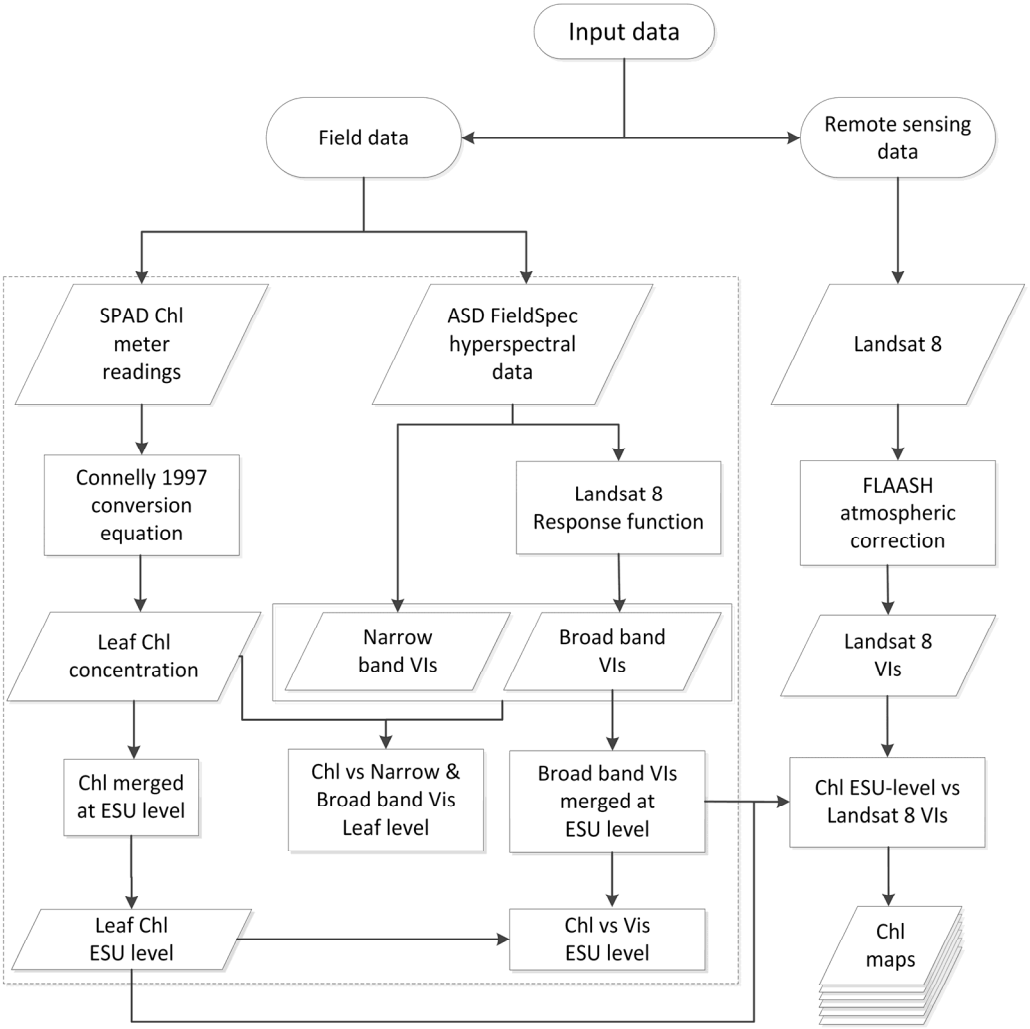

Figure 2. Schematic diagram of the procedures in relating CC to VIs. In this paper the leaf level refers to the CC and hyperspectral response measured at individual leaves. ESU level refers to CC and hyperspectral response averaged at Elementary Sampling Unit level (a plot of 30 m by 30 m to represent the spatial resolution of Landsat 8). Chl maps were computed using the Landsat 8 VI, which had the best performance in terms of correlation with Chl at ESU level.

2.3. Ground Data Processing

2.3.1. SPAD Calibration

Several equations describing the statistical relationship between the SPAD readings and CC are available in the literature. We used the homographic equation of Connelly (1997) for *R. mangle* to

convert the SPAD readings to CC. Table S1 in the Supplementary Information shows the published conversion equations including polynomial, exponential, linear, and homographic. The relationship depends on leaf structure factors such as leaf thickness, leaf mass per area (LMA) [28], and the proportion of vascular tissue [59], characteristics known to vary among species. Equations reported by Coste *et al.* [28], Cerovic *et al.* [59], and Marenco *et al.* [60] have general applicability as they are estimated from different species covering a range of leaf characteristics. For the particular case of mangroves, the only equation reported in the literature is that of Connelly [30], established for the red mangrove (*R. mangle*). This equation has a close agreement with equations estimated from different species covering a range of leaf characteristics (Figure S1, Supplementary Information) and, therefore, was deemed to be suitable for the purposes of the study. Once SPAD readings were converted to CC, each individual leaf CC was compared with its corresponding spectral response to establish the CC and spectral characteristics at the leaf level.

Table 1. Hyperspectral and broad band indices used in this research.

Vegetation Index	Abbreviation	Formula	Reference
Simple Ratio Index$_{680}$	SR_{680}	$\frac{\rho 800}{\rho 680}$	[61]
Simple Ratio Index$_{750}$	SR_{750}	$\frac{\rho 750}{\rho 705}$	[62]
Normalized Difference Vegetation Index$_{680}$	$NDVI_{680}$	$\frac{(\rho 800 - \rho 680)}{(\rho 800 + \rho 680)}$	[63]
Normalized Difference Vegetation Index$_{705}$	$NDVI_{705}$	$\frac{(\rho 750 - \rho 705)}{(\rho 750 + \rho 705)}$	[62]
Modified Red Edge Simple Ratio Index	mSR_{705}	$\frac{(\rho 750 - \rho 445)}{(\rho 705 - \rho 445)}$	[45]
Modified Normalized Difference Vegetation Index	mND_{705}	$\frac{(\rho 750 - \rho 705)}{(\rho 750 + \rho 705 - 2 \times \rho 445)}$	[45]
MERIS Terrestrial Chlorophyll Index	MTCI	$\frac{(\rho 753.75 - \rho 708.75)}{(\rho 708.75 + \rho 681.25)}$	[40]
Vogelmann Red Edge Index $_1$	VOG_1	$\frac{\rho 740}{\rho 720}$	[64]
Vogelmann Red Edge Index $_2$	VOG_2	$\frac{(\rho 734 - \rho 747)}{(\rho 715 + \rho 726)}$	[65]
Vogelmann Red Edge Index $_3$	VOG_3	$\frac{(\rho 734 - \rho 747)}{(\rho 715 + \rho 720)}$	[65]
Photochemical Reflectance Index	PRI	$\frac{(\rho 531 - \rho 570)}{(\rho 531 + \rho 570)}$	[66]
Transformed Chlorophyll Absorption Ratio Index	TCARI	$3 \times \left[(\rho 700 - \rho 670) - 0.2 \times (\rho 700 - \rho 550) \times (\frac{\rho 700}{\rho 670})\right]$	[67]
Modified Chlorophyll Absorption Index	$mCARI_{705}$	$[(\rho 750 - \rho 705) - 0.2 \times (\rho 750 - \rho 550)] \times (\frac{\rho 750}{\rho 705})$	[68]
Green Normalized Difference Vegetation Index	NDVI green	$\frac{(\rho NIR - \rho Green)}{(\rho NIR + \rho Green)}$	[69]
Simple Ratio	Simple Ratio	$\frac{\rho NIR}{\rho Red}$	[61]
Green Chlorophyll Index	CI green	$\frac{\rho NIR}{\rho Red} - 1$	[44]
Normalized Difference Vegetation Index	NDVI	$\frac{(\rho NIR - \rho Red)}{(\rho NIR + \rho Red)}$	[63]
Enhanced Vegetation Index	EVI_1	$2.5 \times \frac{(\rho NIR - \rho Red)}{(1 + \rho NIR + 6 \times \rho Red - 7.5 \times \rho Blue)}$	[70]
Enhanced Vegetation Index 2	EVI_2	$2.5 \times \frac{(\rho NIR - \rho Red)}{(1 + \rho NIR + 2.4 \times \rho Red)}$	[71]
Wide Dynamic Rage Vegetation Index	WDRVI	$\frac{(\alpha \times \rho NIR - \rho Red)}{(\alpha \times \rho NIR + \rho Red)}$	[72]
Green Wide Dynamic Range Vegetation Index	WDRVI green	$\frac{(\alpha \times \rho NIR - \rho Green)}{(\alpha \times \rho NIR + \rho Green) + \frac{(1-\alpha)}{(1+\alpha)}}$	[73]

2.3.2. Hyperspectral Data Processing

A total of 21 VIs were computed using the hyperspectral data collected in the field, 13 VIs were narrow band indices while 8 were broad band indices (Table 1). Hyperspectral bands employed were 445, 531, 550, 570, 670, 680, 681, 700, 705, 708, 715, 720, 726, 734, 740, 747, 750, 753, and 800 nm. Spectral bands used to compute broad band VIs were: Blue (436–528), green (512–610), red (625–691), and NIR (829–900 nm). Broad band VIs were computed using the Landsat 8 spectral response function available in the Landsat Science website (http://landsat.gsfc.nasa.gov/). Narrow and broad band indices were then used to establish the relationship between CC and the spectral characteristics of mangrove leaves. Therefore, the selection of these indices was based upon their tested ability to predict CC.

2.4. Satellite Sensor Data Processing

Six Landsat 8 images were obtained between April 2013 and March 2014 (path 21, row 45). All images were pre-processed using the Fast Line-of-sight Atmospheric Analysis of Hypercubes (FLAASH) algorithm in ENVI 5.0. The January 2014 image, which corresponds to the month where field data were obtained, was employed to compute eight broad band VIs: NDVI green, WDRVI green, NDVI, EVI_2, WDRVI, CI green, SR, and EVI_1 (Table 1). These VIs produced a large correlation with CC from previous analyses. The correlation between CC at the ESU level and Landsat 8 VIs was examined. The index that provided the largest correlation between the Landsat 8 images and CC measured at the ground was then used to produce the CC maps. Non-mangrove pixels were masked out using the land cover map of the Yucatan Peninsula [74].

Statistical Analysis

The Kruskal–Wallis test was conducted to explore the overall statistical difference among mangrove species. Further, pairwise comparisons between species were conducted using the Wilcoxon signed-rank test. To establish the relationship between leaf CC and leaf spectral response, simple linear regression was applied and the coefficient of determination was estimated for the entire dataset and on a per-species basis. To examine the influence of a mixed species signal and its relationship with CC, CC and the VIs were merged at each ESU and simple linear regression was applied and the coefficient of determination estimated. Similarly, to examine the relationship between CC measured at the ground and Landsat 8 VIs, the CC was merged at each ESU and simple linear regression was applied and the coefficient of determination estimated. The LOOCV approach was used to assess the accuracy of the CC map created with the image acquired close to the field campaign dates, and the coefficient of determination and RMSE were estimated. This LOOCV approach consists of training a model with the complete dataset except for one point, then that point is predicted by the model allowing accuracy statistics to be estimated. The process iterates N times and the RMSE is calculated [75]. Statistical analyses were conducted in the R statistical software [76].

3. Results

3.1. Spectral Variation among Species

Spectral reflectance curves of the four mangrove species are presented in Figure 3. In general, the species exhibit similar curves typical of green vegetation. *A. germinans* had the highest reflectance in the visible region as well as in the NIR, while *R. mangle* had the lowest reflectance in the visible spectral bands. *C. erectus* and *A. germinans* are not clearly distinguishable in the green region. Similarly, *R. mangle* and *C. erectus* are confounded in the NIR region of the spectrum.

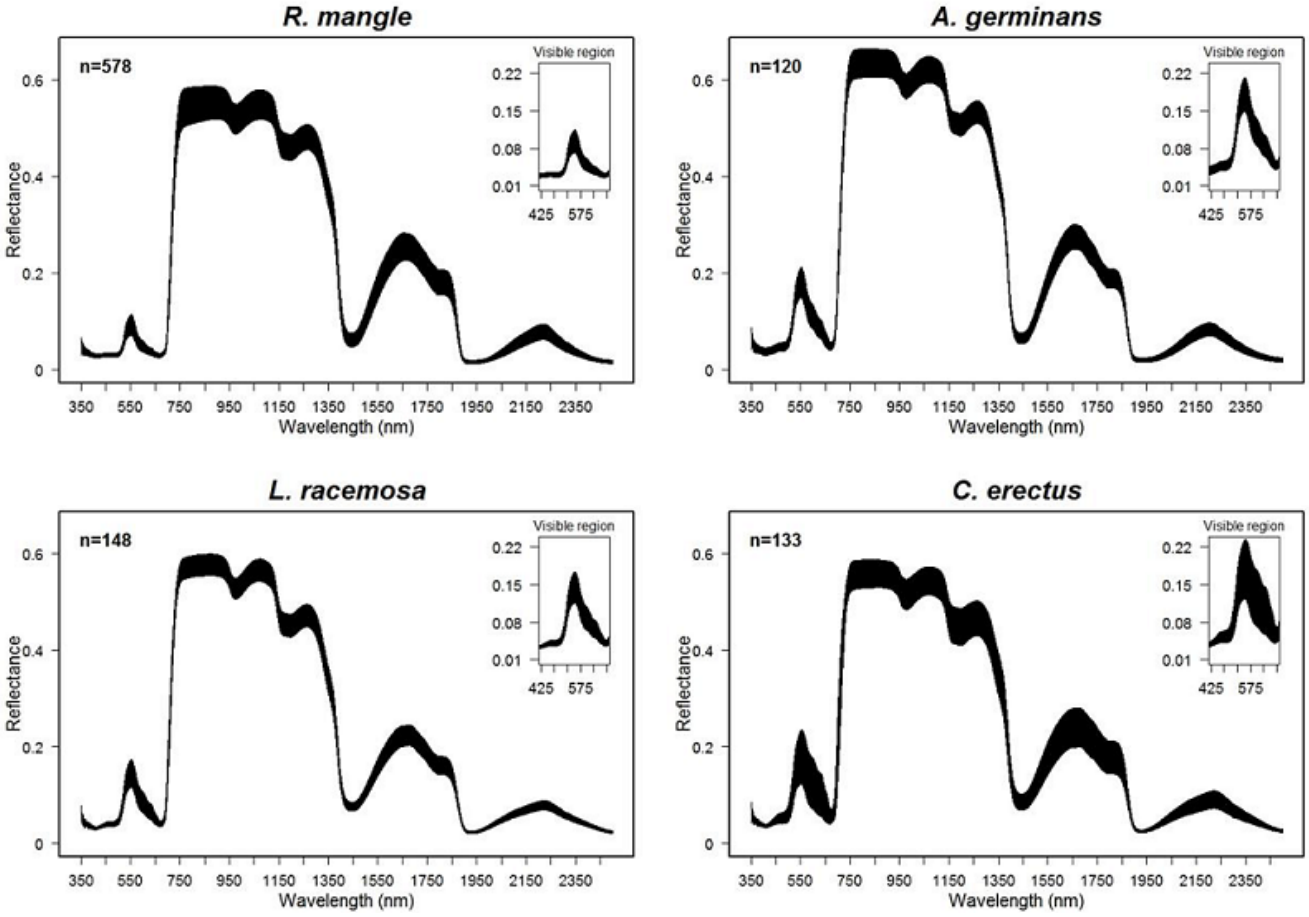

Figure 3. Spectral reflectance of mangrove species (mean ± SD). The smaller plots on the upper right corner represent a zoom in of the visible range of the spectrum. The visible region depicts features associated with differences in Chl ($\mu g \cdot cm^{-2}$) among species. *R. mangle*, the species with the highest CC shows the lower reflectance in the visible part of the spectrum.

3.2. Mangrove Species CC

Figure 4 shows the CC in leaves obtained from four species of mangrove. The range of CC was 2.28–92.28 $\mu g \cdot cm^{-2}$ for *C. erectus*, 16.67–84.39 $\mu g \cdot cm^{-2}$ for *L. racemosa*, 20.35–82.81 $\mu g \cdot cm^{-2}$ for *A. germinans*, and 22.28–96.14 $\mu g \cdot cm^{-2}$ for *R. mangle*. On average, CC was highest for *R. mangle* and lowest for *C. erectus*. Significant differences ($p < 0.05$) were observed between the following pairs: (i) *R. mangle–A. germinans*, (ii) *L. racemosa–C. erectus*, and (iii) *R. mangle–C. erectus*.

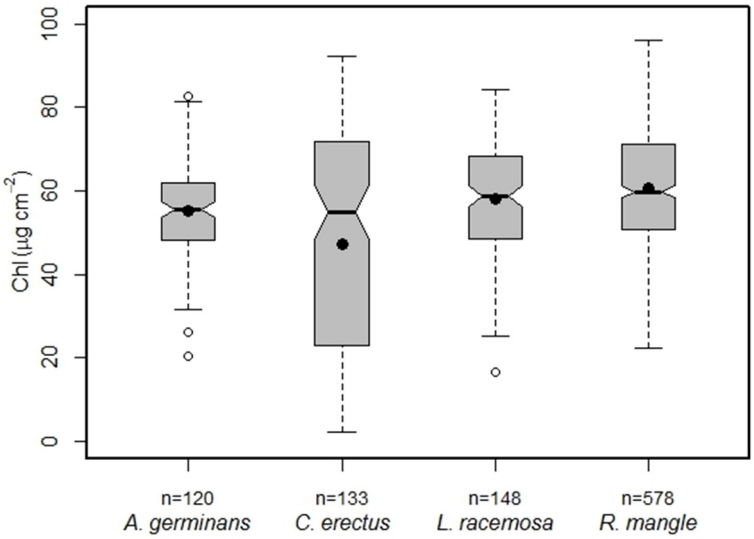

Figure 4. Leaf CC (µg·cm^{-2}) for the four mangrove species. Each box embodies the first and the third quartile. The bold line represents the median while the dark dot represents the mean. Whiskers are located at 1.5 times the interquartile range and white dots denote outliers. Significant differences ($p < 0.05$) were observed between the following pairs: (i) *R. mangle–A. germinans*, (ii) *L. racemosa–C. erectus*, and (iii) *R. mangle–C. erectus*.

3.3. Performance of VIs

Leaf hyperspectral response was used to derive the VIs listed in Table 1. Leaf-level relationships were computed between the narrow band VIs and CC. The narrow band VIs with the most explanatory power ($R^2 > 0.5$) were VOG indices, MTCI, mND_{705}, mSR_{705}, $mCARI_{705}$, and SR_{750} (Table 2, Figure 5). When coefficients of determination were computed on a per-species basis, VIs followed the same trend showing an increase in the percentage of explained variation in CC. The best performing narrow band VIs in terms of coefficient of determination for *R. mangle* were VOG_2, VOG_3, VOG_1, mND_{705}, and MTCI (Table 3). Similarly, VOG_2, VOG_3, MTCI, VOG_1, and mSR_{705} performed best for *L. racemosa* (Table 4). *A. germinans* CC had the largest correlation with VOG_1, VOG_3, mCARI705, MTCI, and mND_{705} (Table 5), while VOG_2, VOG_3, VOG_1, $mCARI_{705}$, and mND_{705} best explained CC variation in *C. erectus* (Table 6).

Table 2. Relationship between CC and VIs ($n = 987$).

VI	Intercept	Slope	R^2	RMSE	Signif.
VOG_2	20.382	−449.057	0.588	11.3	***
VOG_1	−77.714	91.798	0.587	11.3	***
VOG_3	22.558	−379.752	0.582	11.4	***
MTCI	22.817	15.554	0.564	11.7	***
mND_{705}	−7.524	112.029	0.551	11.8	***
mSR_{705}	16.172	10.088	0.530	12.1	***
$mCARI_{705}$	22.597	35.201	0.528	12.1	***
SR_{750}	9.051	14.264	0.514	12.3	***
TCARI	82.556	−103.717	0.457	13.0	***

Table 2. *Cont.*

VI	Intercept	Slope	R^2	RMSE	Signif.
WDRVI green	15.381	65.250	0.450	13.1	***
NDVI green	2.228	92.202	0.446	13.2	***
CI green	30.693	7.828	0.432	13.3	***
NDVI	−40.481	120.412	0.281	15.0	***
WDRVI	27.422	60.234	0.274	15.1	***
SR	30.901	2.438	0.217	15.6	***
EVI2	−30.779	228.633	0.203	15.8	***
EVI1	−34.546	221.288	0.198	15.8	***
$NDVI_{705}$	10.544	116.844	0.185	16.0	***
SR_{680}	32.193	1.614	0.116	16.6	***
$NDVI_{680}$	40.587	30.073	0.006	17.6	*

Notes: Statistical significance 0.05 "*"; 0.001 "***".

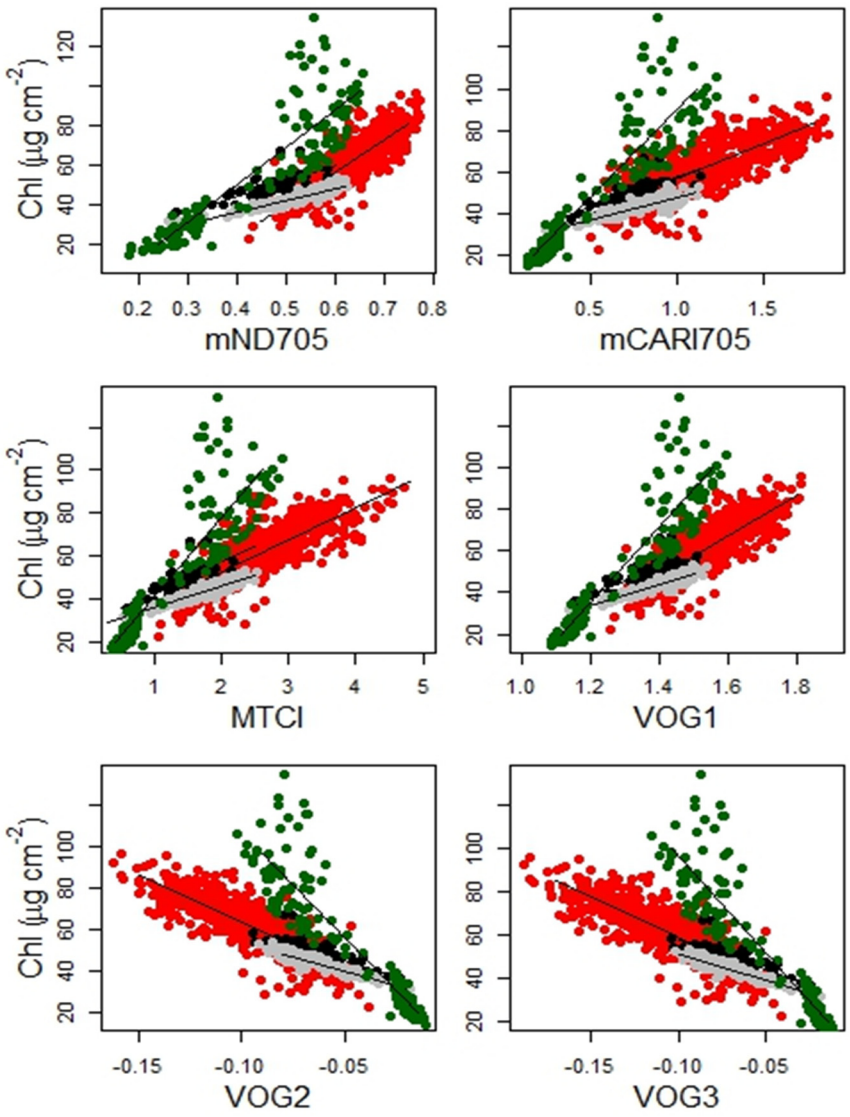

Figure 5. Scatterplots of VIs that showed the highest correlation ($R^2 > 0.53$) with CC. Red: *R. mangle*, black: *A. germinans*, grey: *L. racemosa*, and green: *C. erectus*.

Table 3. Relationship between CC and VIs for *R. mangle* (*n* = 579).

VI	Intercept	Slope	R^2	RMSE	Signif.
VOG_2	18.188	−451.792	0.693	5.7	***
VOG_3	21.345	−373.644	0.688	5.7	***
VOG_1	−87.574	96.967	0.672	5.8	***
mND_{705}	−42.674	163.958	0.672	5.8	***
MTCI	22.359	15.054	0.670	5.9	***
mSR_{705}	14.913	9.963	0.650	6.0	***
SR_{750}	4.131	15.024	0.621	6.3	***
NDVIgreen	−54.493	174.230	0.609	6.4	***
WDRVIgreen	−13.384	100.923	0.607	6.4	***
CIgreen	24.163	8.929	0.584	6.6	***
$mCARI_{705}$	23.182	33.436	0.582	6.6	***
TCARI	93.665	−174.992	0.577	6.6	***
$NDVI_{705}$	29.339	81.311	0.114	9.6	***
WDRVI	31.829	51.978	0.056	10.0	***
SR	44.576	1.352	0.055	10.0	***
NDVI	−43.281	123.583	0.055	10.0	***
EVI_1	15.393	110.420	0.043	10.0	***
EVI_2	20.601	104.767	0.037	10.1	***
$NDVI_{680}$	44.377	33.138	0.011	10.2	**
SR_{680}	60.735	0.049	0.000	10.2	ns

Notes: Statistical significance, not significant "ns"; 0.05 "*"; 0.01 "**"; 0.001 "***".

Table 4. Relationship between CC and VIs for *L. racemosa* (*n* = 151).

VI	Intercept	Slope	R^2	RMSE	Signif.
VOG_2	26.277	−274.101	0.881	0.6	***
VOG_3	27.114	−238.934	0.880	0.6	***
MTCI	26.178	10.039	0.866	0.6	***
VOG_1	−26.703	50.467	0.865	0.6	***
mSR_{705}	19.105	7.395	0.852	0.7	***
CI green	27.373	6.728	0.841	0.7	***
SR_{750}	15.436	9.852	0.838	0.7	***
TCARI	60.562	−57.535	0.835	0.7	***
mND_{705}	12.596	58.631	0.830	0.7	***
WDRVI green	21.085	41.491	0.830	0.7	***
NDVI green	14.663	53.726	0.809	0.8	***
$mCARI_{705}$	26.561	21.353	0.804	0.8	***
WDRVI	24.994	41.655	0.545	1.2	***
SR	23.427	2.278	0.541	1.2	***
NDVI	−22.222	82.947	0.536	1.2	***
EVI_1	−13.213	135.008	0.422	1.4	***
EVI_2	−10.006	138.282	0.420	1.4	***
$NDVI_{705}$	16.729	65.825	0.384	1.4	***
SR_{680}	29.778	0.964	0.139	1.7	***
$NDVI_{680}$	19.155	43.457	0.059	1.7	**

Notes: Statistical significance, 0.01 "**"; 0.001 "***".

Table 5. Relationship between CC and VIs for *A. germinans* (n = 121).

VI	Intercept	Slope	R^2	RMSE	Signif.
VOG_2	29.348	−309.760	0.639	0.9	***
VOG_3	30.320	−273.024	0.634	0.9	***
$mCARI_{705}$	28.267	29.045	0.627	0.9	***
MTCI	28.543	14.332	0.594	1.0	***
mND_{705}	12.727	77.113	0.590	1.0	***
VOG_1	−34.331	61.339	0.589	1.0	***
mSR_{705}	17.873	11.066	0.579	1.0	***
SR_{750}	16.139	13.104	0.523	1.0	***
EVI1	−17.632	152.880	0.492	1.0	***
EVI2	−16.545	164.050	0.452	1.1	***
NDVI green	26.849	47.782	0.384	1.2	***
WDRVI green	32.141	38.064	0.372	1.2	***
TCARI	66.330	−42.785	0.362	1.2	***
CI green	37.155	6.625	0.346	1.2	***
$NDVI_{705}$	21.378	59.379	0.258	1.3	***
NDVI	14.489	45.855	0.188	1.3	***
WDRVI	40.738	22.664	0.175	1.3	***
$NDVI_{680}$	13.451	58.514	0.136	1.4	**
SR	40.683	1.125	0.127	1.4	**
SR_{680}	39.332	0.765	0.077	1.4	*

Notes: Statistical significance, 0.05 "*"; 0.01 "**"; 0.001 "***".

Table 6. Relationship between CC and VIs for *C. erectus* (n = 136).

VI	Intercept	Slope	R^2	RMSE	Signif.
VOG_2	4.968	−1013.500	0.834	5.0	***
VOG_3	6.924	−895.743	0.830	5.0	***
VOG_1	−182.561	181.758	0.817	5.2	***
$mCARI_{705}$	6.077	84.213	0.810	5.3	***
mND_{705}	−26.193	188.601	0.794	5.5	***
EVI2	−146.001	602.331	0.794	5.5	***
EVI1	−144.589	545.121	0.783	5.7	***
MTCI	4.549	36.791	0.779	5.7	***
$NDVI_{705}$	−58.082	335.829	0.776	5.8	***
SR_{750}	−34.070	37.251	0.775	5.8	***
mSR_{705}	−20.928	27.366	0.768	5.9	***
SR_{680}	−64.088	12.103	0.755	6.0	***
NDVI green	−23.472	188.194	0.735	6.3	***
WDRVI green	−7.665	157.046	0.726	6.4	***
WDRVI	19.586	143.564	0.711	6.6	***
NDVI	−116.197	250.425	0.705	6.6	***
CI green	7.468	28.715	0.698	6.7	***
TCARI	130.880	−201.672	0.686	6.8	***
SR	−13.847	11.322	0.685	6.8	***
$NDVI_{680}$	−253.313	605.497	0.501	8.6	***

Notes: Statistical significance, 0.001 "***".

3.4. VIs and CC at the ESU Level

The CC of sampled leaves and narrow band VIs were averaged within the ESUs. The main difference between this step and the previous section is that in this section we attempted to produce a mixed species response. Linear models were fitted to describe quantitatively the response of VIs to change in CC at the ESU level. The red-edge VIs mCARI, VOG_1, EVI_2, EVI_1, VOG_2, VOG_3, mND, NDVI, SR_{750}, MTCI, mSR, and NDVI green individually explained more than 60% of the variation in CC (Figure 6). It is important to note that some of these indices (NDVI green, WDRVI green, NDVI, EVI_2, WDRVI, CI green, SR, and EVI_1) can be calculated using Landsat 8 data, allowing measurements of chlorophyll concentration at landscape scale.

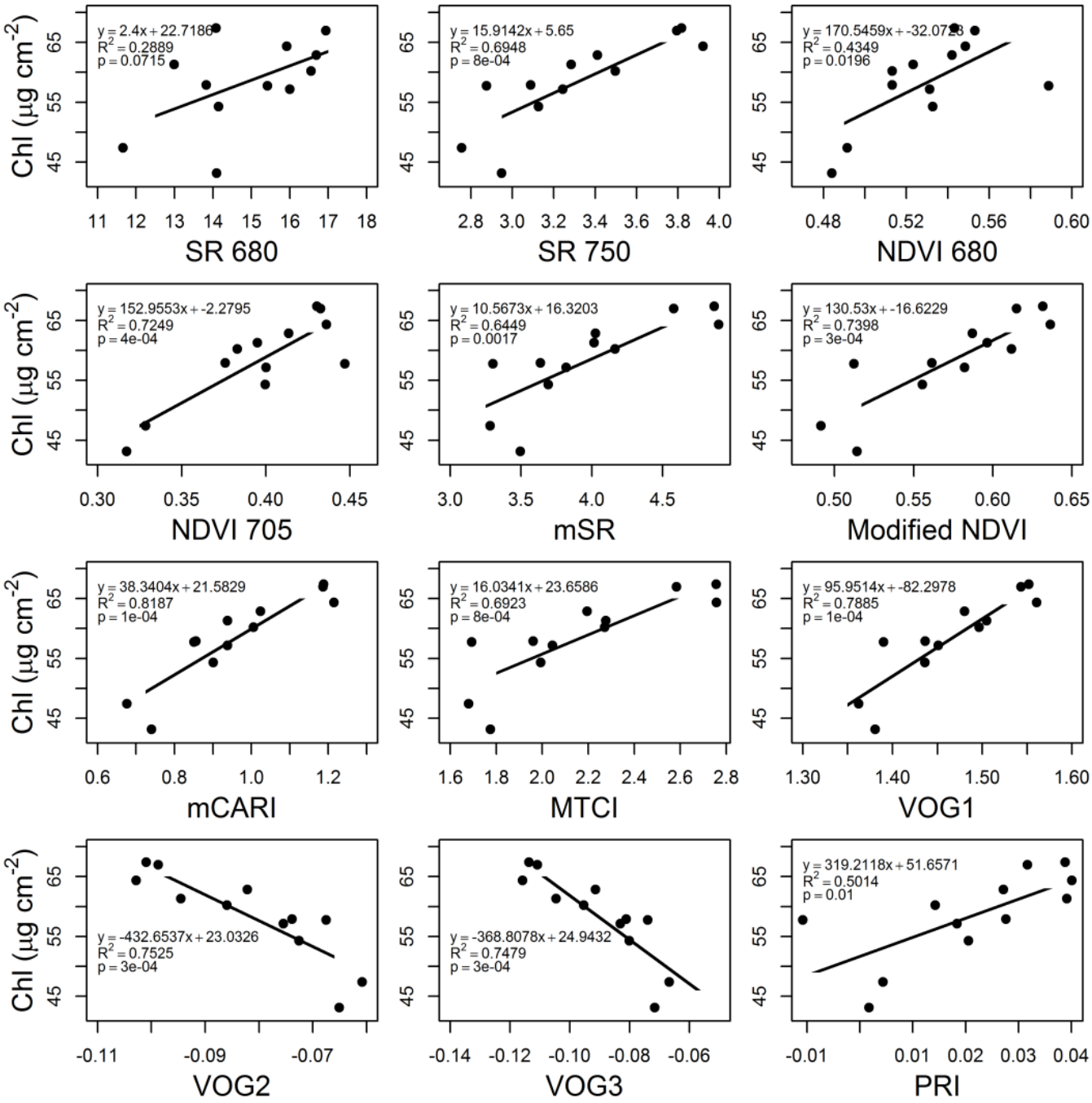

Figure 6. *Cont.*

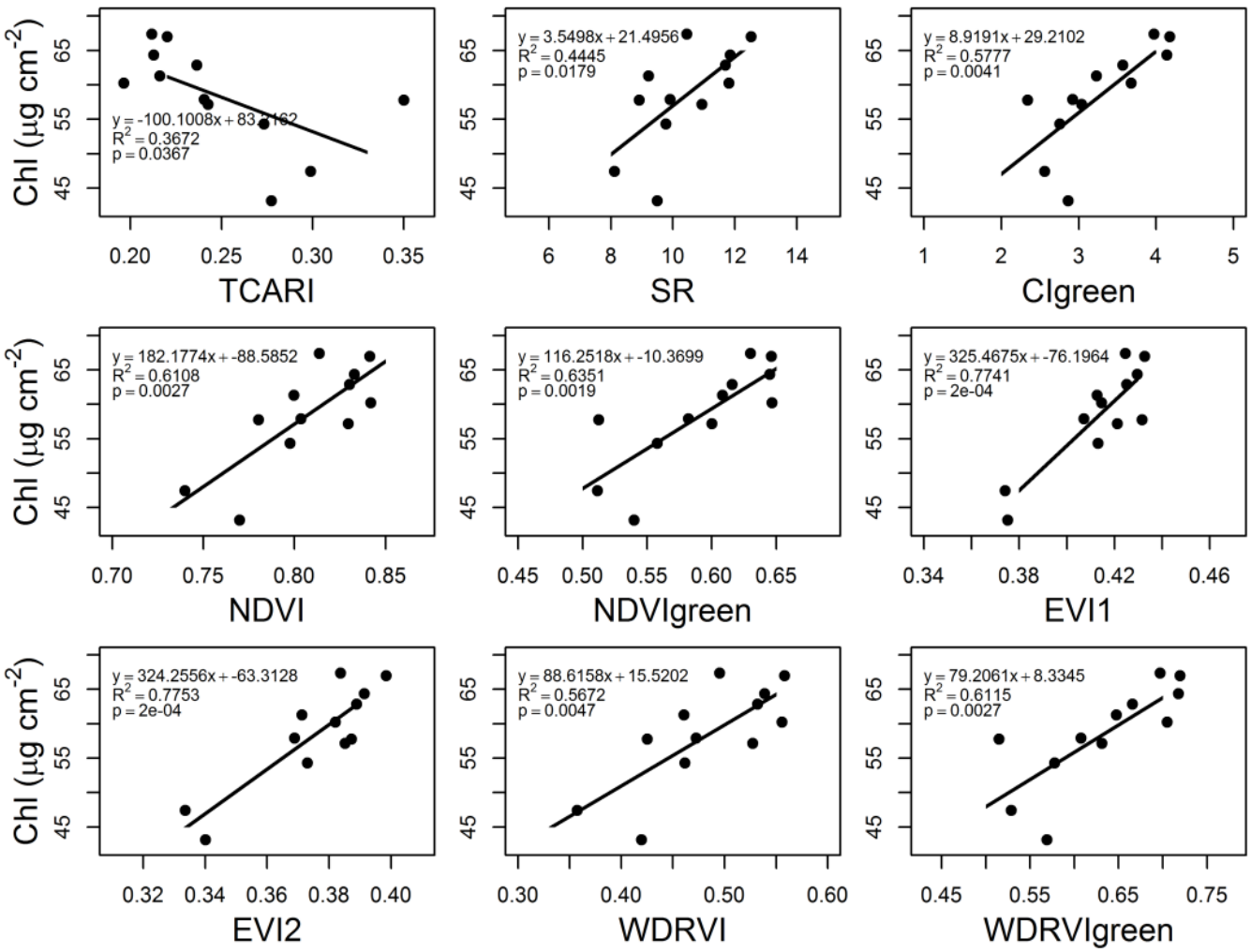

Figure 6. Correlations between VIs and CC (µg·cm^{-2}) at ESU level.

3.5. Chl Concentration and Landsat 8 VIs

One Landsat 8 image acquired in January 2014 was used to derive broad band VIs for comparison with CC at the ESU level. Using the coordinates recorded in the field, each ESU plot was located on the Landsat 8 image. The average CC per ESU was plotted against its corresponding pixel on the Landsat 8 NDVI green and the coefficient of determination was computed. The correlation analyses demonstrated that Landsat 8 NDVI green is the broad band VI most sensitive to CC at the ESU level (R^2 = 0.805), (Figure 7). The linear model that produced this large correlation, described by Equation 1, was used to construct a Chl map.

$$y = -54.545 + 149.396x \quad (1)$$

where x = pixel value of the Landsat 8 NDVI green image.

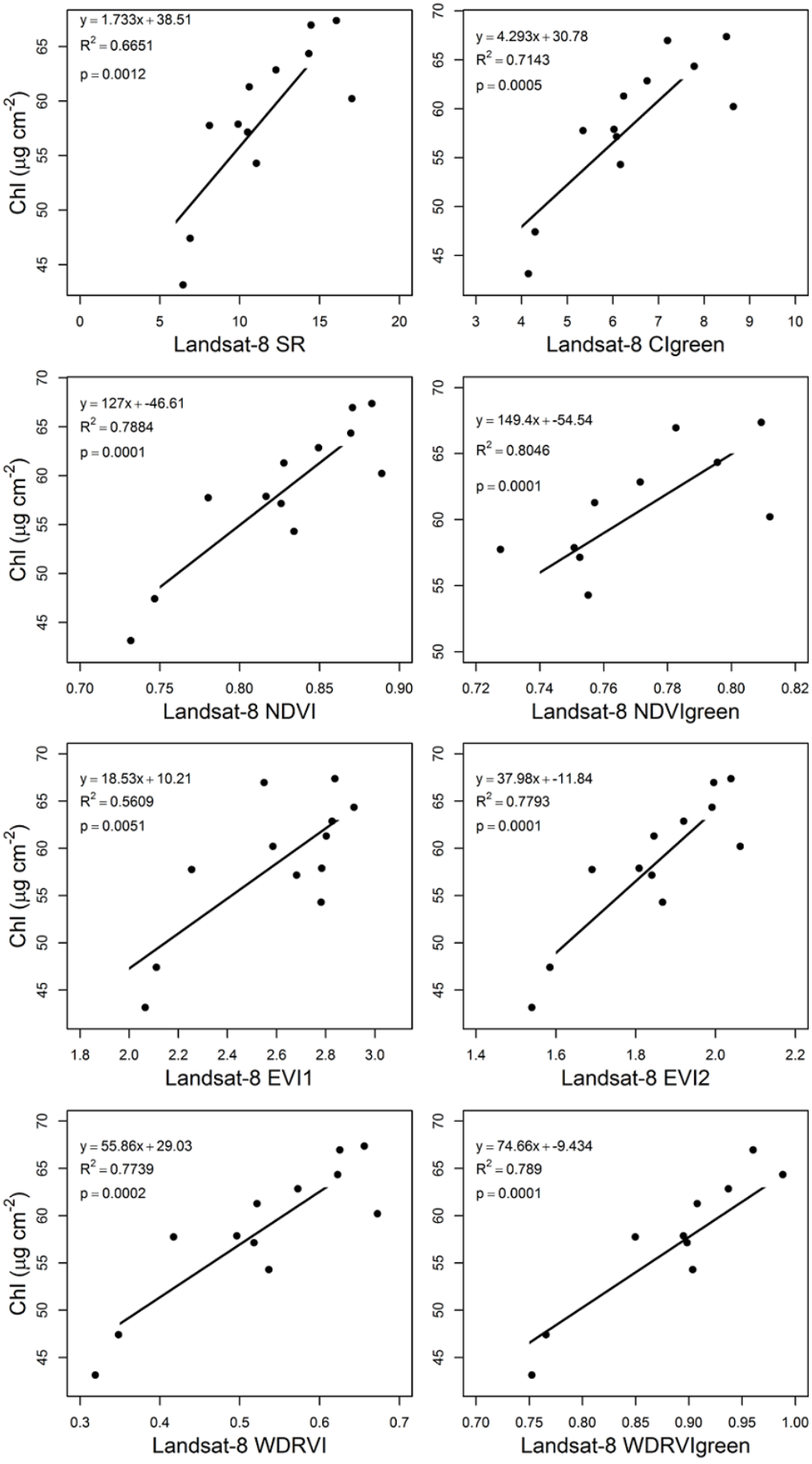

Figure 7. Correlations between Landsat 8 VIs and CC at ESU level.

3.6. Accuracy Assessment

The relationship between CC at the ESU level and Landsat 8 NDVI green expressed by Equation (1) was assessed using the LOOCV method. The coefficient of determination was relatively large (R^2 = 0.703) indicating a good level of agreement between observed CC and predicted CC (Figure 8). The root mean squared error (RMSE) was used to compare the observed *vs.* predicted CC (RMSE = 15 g·cm^{-2}). RMSE was calculated using Equation (2):

$$RMSE = \sqrt{\frac{\sum_{i=1}^{n}(CCobs_i - CCpred_i)^2}{n}}, \quad (2)$$

where CCobs and CCpred are the observed and predicted CC, respectively.

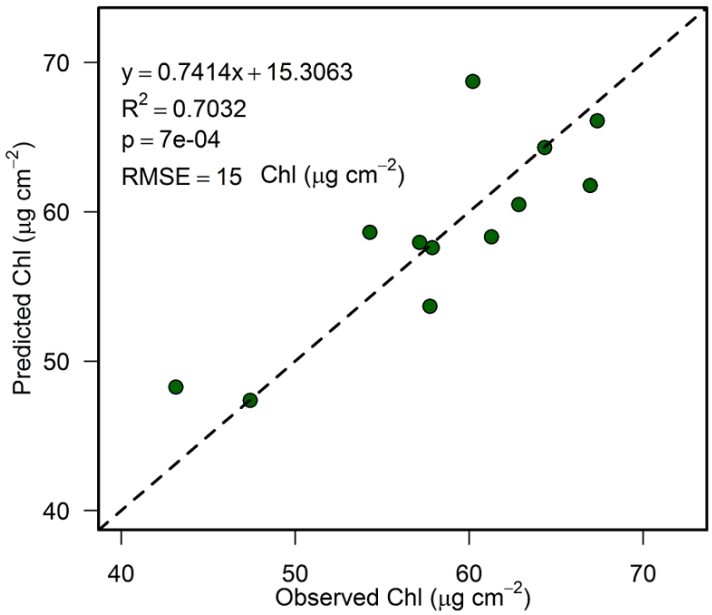

Figure 8. Observed against predicted CC using the leave-one-out cross-validation method. Each point represents an ESU. RMSE =15 µg·cm^{-2}, R^2 = 0.703.

3.7. Spatial Variation of Chlorophyll Concentration across the Study Site

A Landsat 8 image acquired in January 2014 was used to produce landscape scale mangrove leaf CC map. First, NDVI green was computed for the region of interest then, using Equation (1), CC was calculated for every pixel using the band math tool in ENVI 5.0. The same procedure was applied to the Landsat 8 images acquired at different dates throughout a complete annual cycle (Figure 9). Maps are able to show the spatial distribution of CC with a pattern that seems related to distance from water. Larger CC values are observed at the borders of the Ría Celestún, in petenes (characterized by circular shaped "islands" of vegetation), and flooded areas, with values decreasing towards the continent or the sea. With respect to the temporal variability, in general the maps depict an increasing gradient from April 2013 to November 2013 and a decreasing pattern form November 2013 to March 2014 (Figure 10).

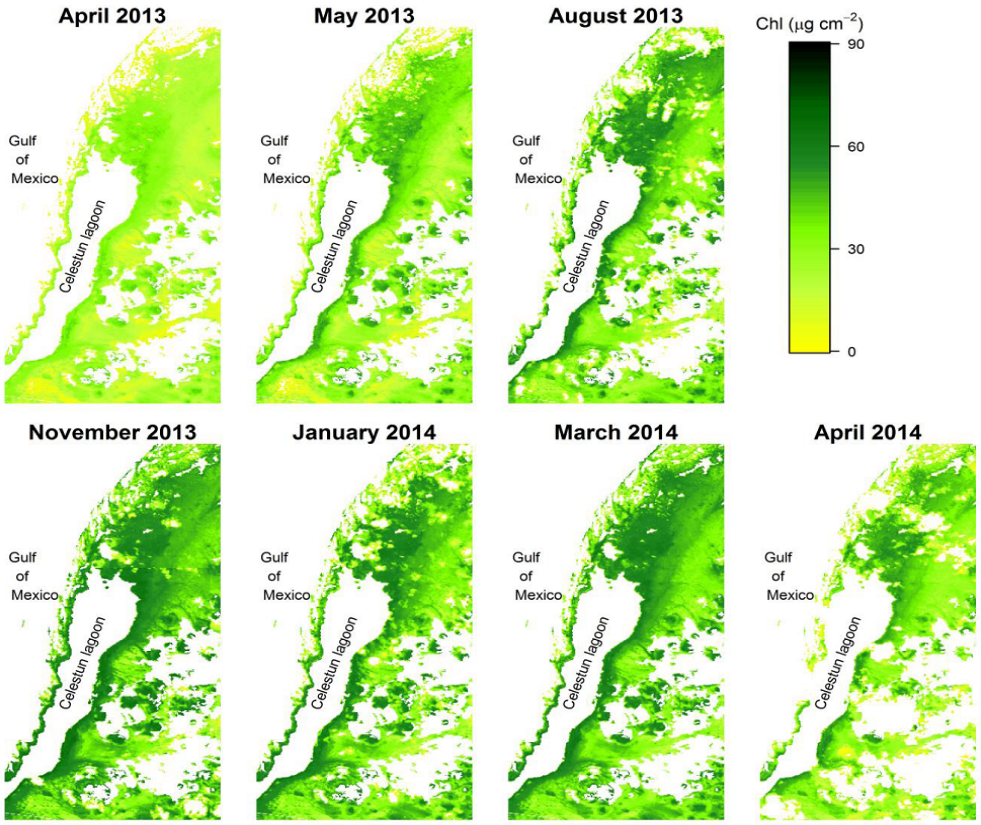

Figure 9. Remote sensing-based maps of the spatiotemporal variation in CC (µg·cm^{-2}) estimated using the relationship between Landsat 8 NDVI green and Chl measurements obtained in the field. The non-mangrove pixels have been masked out.

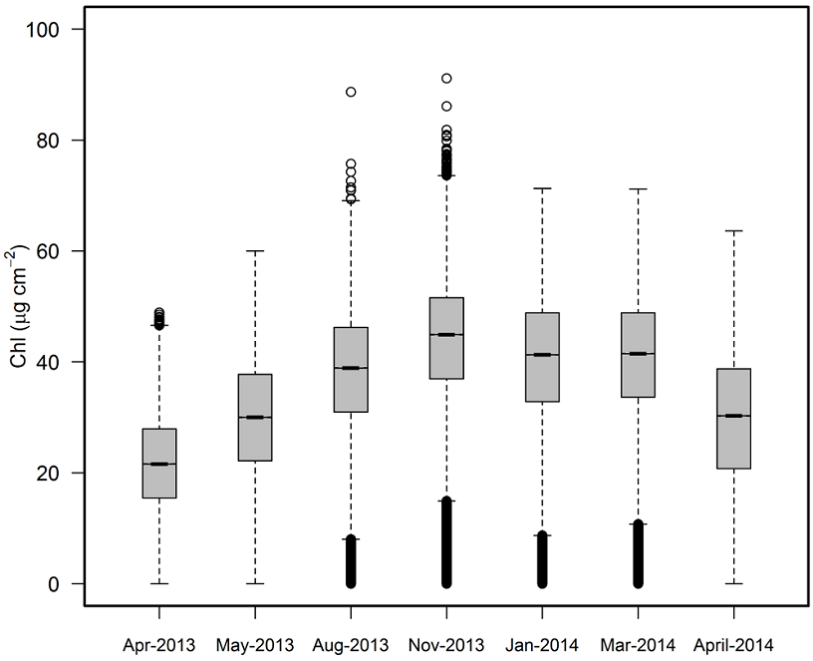

Figure 10. Temporal variation in CC. The boxes represent each CC map. Each box embodies the first and the third quartile. The bold line represents the median while the dark dot represents the mean. Whiskers are located at 1.5 times the interquartile range and white dots denote outliers.

4. Discussion

Leaf CC is an important biophysical variable used as an indicator of vegetation condition and stress. Field-based measurements of biophysical variables in mangrove forests are labor-intensive and time-consuming. Consequently, only a few spatially localized studies have focused on estimating mangrove CC [21,22,32]. To obtain a synoptic view of mangrove condition at the landscape level, it is important to generate more data on the spatial and temporal variation of mangrove biochemical variables. The current research assessed the performance of hyperspectral and broad band VIs for predicting the CC of mangroves at the leaf and ESU levels. The association between CC at the ESU level and Landsat 8 NDVI green was validated using the LOOCV approach. In addition, six maps depicting the spatiotemporal variability of CC using Landsat 8 data are presented.

4.1. Spectral Signature and Chl Concentration

Leaf spectral features in the visible and NIR regions of the spectrum have been associated to pigment concentration (e.g., chlorophyll) and leaf structure, respectively [77]. Chl peaks of absorbance are located in the blue and red regions of the spectrum. Since carotenoid absorbance also occurs in the blue region, typically the red spectral bands are used to estimate Chl [45]. Low reflectance in the red part of the spectrum is then related to the presence of Chl. In this study, *R. mangle* had the lowest reflectance in the red spectral bands, followed by *L. racemosa*, *A. germinans*, and finally *C. erectus* with the highest reflectance of the four species. Accordingly, the average CC followed the same gradient; it was highest for *R. mangle* and lowest for C. erectus, no statistical difference was found between *L. racemosa* and *A. germinans* and *R. mangle* and *L. racemosa*. Likewise, Flores-de-Santiago, Kovacs and Flores-Verdugo [22,32] reported similar CC ranges per species; the highest CC in *R. mangle* and lowest for *L. racemosa* and *A. germinans* was in the Mexican Pacific. In Brazil, Rebelo-Mochel and Ponzoni [78] reported the highest reflectance in the visible bands for *C. erectus* and lowest for *R. mangle*, confirming our results. However, they did not measure pigment concentration.

The NIR reflectance, in contrast, is known to be affected by leaf anatomical structure such as leaf thickness, cell walls, and intracellular air spaces. We did not carry out leaf anatomical measurements; however, the low NIR reflectance of *R. mangle* and significantly higher reflectance of *A. germinans* would suggest differences in leaf morphological characteristics. Rebelo-Mochel and Ponzoni [78] also reported higher reflectance in the NIR for *A. germinans*. In addition, Lima *et al.* [79] reported significantly lower palisade, spongy parenchyma, and total leaf thickness for *R. mangle*. Furthermore, physical gradients such as waterlogging [80] and salinity [81–83] act on mangrove leaf morphology and pigment concentration and this, in turn, could affect the visible and NIR leaf reflectance.

4.2. Chl Concentration and Narrow Band Vegetation Indices

In general, the correlation between the VIs derived from remote sensing data and CC in the mangrove leaves was significant at all levels. Indices specifically designed to be sensitive to CC such as VOG indices and MTCI produced the largest coefficient of determination at the leaf level ($R^2 > 0.5$).

VIs that best explained the variability in CC were those that included in their formula spectral bands in the range 705 to 753 nm (e.g., VOG and MTCI). VOG indices and MTCI had the largest correlation

with CC at the leaf level (R^2 = 0.56–0.58) when all leaves were pooled together. Similarly, these indices had the largest correlation on a per-species basis (Tables 3–6, Figure 5). Flores-de-Santiago, Kovacs and Flores-Verdugo [32] and Zhang [19] suggested VOG_1 was the optimal VI in terms of its linear correlation with Chl a concentration in mangrove leaves. Moreover, our results show that the MTCI had equal or, in some cases, larger correlation with leaf CC than VOG_1. For instance, VOG_1 had an average difference of 1.1% with respect to MTCI. Also, in this study VOG_2 correlated better with CC than VOG_1 or MTCI. Finally, opposed to their counterparts, the modified indices mSR_{705}, mND_{705}, and $mCARI_{705}$ produced a larger correlation. Modified indices with spectral bands of 705 nm and 750 nm in general had a larger correlation than those composed by 800 nm and 670 nm [68]; this is consistent with our findings in that mND_{705} performed at the same level of VOG indices in *R. mangle*, the species with the highest CC.

4.3. Chl Concentration and Broad Band Vegetation Indices Performance from Leaf to ESU Level

According to our results, the relationship between broad band VIs and CC increased as we move from leaf level to ESU level (Figure 7). Although the correlation between CC and broad band VIs was significant at leaf level (Table 2), this correlation was relatively weak ($R^2 \sim 0.4$, $p < 0.001$). The relatively weak relationship is explained by the variability in the data. Differences in leaf structure among mangrove species affect the leaf spectral reflectance. Therefore, the response of VIs to CC varies among mangrove species (Tables 3–6). Conversely, at ESU level, high significant correlation was observed between six Landsat 8 broad band VIs and CC ($N = 12$; $R^2 > 0.7$; $p < 0.001$). At this stage, the CC measured at each ESU was averaged and compared with the Landsat 8 broad VI pixel value. In this study, Landsat 8 NDVI green was able to explain ~80% of the variation in CC at the ESU level. The linear model that produced this large correlation was the basis for upscaling CC at landscape scale.

The main difference between broad band and hyperspectral algorithms is the width of the spectral band used for the computation of the index. Broad band indices use information from wide regions of the spectrum such as blue, green, red, near infrared, and short wave near infrared regions. On the contrary, hyperspectral indices include narrow regions of the spectrum. It is possible to derive information about the structure and biochemical composition of vegetation from both types of indices, however, hyperspectral indices that include bands in areas of the spectrum of high absorbance by chlorophyll a and b (particularly between 650 and 690 nm) perform best at estimating chlorophyll concentration. The transition region between the red and the near infrared part of the spectrum, the so-called red edge (680–750 nm) tends to shift towards longer wavelengths at high chlorophyll concentrations [41]; therefore, those indices that include narrow bands in the red edge are more sensitive to variations in chlorophyll.

4.4. Chl Map

The VI that best explained the variation in CC at the ESU level, the Landsat 8 NDVI green, was used to create the Chl maps. Gitelson *et al.* [69] developed the NDVI green for MODIS and, unlike its predecessor, the NDVI that uses the red band (650–690 nm), the NDVI green incorporates the green band (530–570 nm) in its formulation and is sensitive to a wider range of CC [69,84]. Similar to MODIS, the Landsat 8 green band ranges between 530 and 590 nm, this region of the electromagnetic spectrum

is located above the "green edge" between two regions of strong pigment absorption: blue (460–480 nm) and red (650–690 nm) [69]. It has been observed that the green edge has behavior similar to the red edge in the sense that both edges tend to shift towards longer wavelengths at high CC [41]. Therefore, as CC increases and the red spectral band reaches minimum reflectance the green band still remains sensitive; this may explain why Landsat 8 NDVI green was best correlated to CC at ESU level.

To our knowledge, this is the first time that Landsat 8 has been used to map the CC of mangrove forest at landscape scale in Mexico. The importance of the relationship between Landsat 8 VIs and CC stems from the potential of Chl to be used as a proxy of GPP, as has been suggested in precision agriculture studies [85,86].

Although the Chl maps depict a reasonable spatial and temporal pattern in CC, there is uncertainty associated to them as they were constructed under some limitations and assumptions. The main limitation of this study is that LAI measurements were not collected during the field campaign. LAI is a major component of canopy Chl content [87,88], this latter is defined as the product of CC and LAI [44,84]. Therefore, in this study it was not possible to derive canopy Chl content to plot against Landsat 8 NDVI green. Instead of canopy Chl content, we used leaf CC averaged at the ESU level.

In addition, differences in plant structure, changes in soil reflectance, and changes in soil moisture and leaf moisture might affect the relationship between Landsat 8 VIs and CC at ESU level [43] particularly at LAI < 3 [89].

Although this assumption requires further investigation, there are reasons to believe that LAI does not vary much temporally. In an evergreen tropical forest Wagner *et al.* [90] reported seasonal variations in EVI and litter fall, but the authors did not find a seasonal pattern in LAI. Similarly, in a mangrove forest in the Mexican Pacific, Flores-de-Santiago, Kovacs and Flores-Verdugo [22] found no significant difference in LAI between dry and rainy seasons for *R. mangle* and *A. germinans*, irrespective of their condition; the authors only found significant difference in LAI in *L. racemosa*. In summary, one major assumption in the present study was that Landsat 8 NDVI green responded to variation in CC at the ESU level rather than to variation in LAI, canopy closure, and background reflectance, suggesting that further research is needed to account for the potential contribution from LAI in CC estimation.

Another assumption was that the trees sampled were representative of a Landsat 8 pixel of 30 m × 30 m. Pixels that cover more than one species are a source of uncertainty [68]. According to our results, mangrove species contribute in different proportions to the total CC at ESU level. Although only four species of mangrove dominate the landscape in the study area, species composition and density vary spatially [91]. It is also important to note that the association between CC and VIs was based on the January image (close to maximum canopy development) with average CC ranging between 40 and 70 $\mu g \cdot cm^{-2}$ thus particularly the low CC values (e.g., those estimated in April/May 2013) are affected by a degree of uncertainty. In addition, in order to convert SPAD readings into actual chlorophyll concentration calibration equations have to be applied; however, due to logistical and equipment constrains in this study it was not possible to derive calibration equations from the SPAD readings. Therefore, a published equation based on the dominant species of mangrove was used.

To partially overcome some of these issues, it is recommended to sample a larger number of ESUs including field measurements of LAI at different seasons and to develop Chl meter and CC calibration equations. Finally, as this is a pioneer study the authors acknowledge that the limited number of ESUs

may lead to optimistic results. For the reasons explained above, in this paper the focus is on the seasonal variation of CC rather than in the absolute values of CC.

The results of this research have implications for the use of a new generation of satellites that include a spectral band in the red edge position such as the Sentinel 2 from the European Space Agency. At a leaf level, the hyperspectral indices tested in this study that had a red edge band in their formulation achieved a larger correlation with leaf CC. At ESU level, the Landsat 8 broad band index NDVI green achieved the largest correlation with Chl measured on the ground. Further, Sentinel 2 will enable computation of commonly used broad band indices such as the NDVI green plus the highly correlated VI's using the red edge bands. Sentinel 2 transcends the capabilities of the Landsat mission in terms of swath width, spatial resolution, revisit time, and number of spectral bands [92]. Information in the red edge combined with the frequent revisit time of Sentinel 2 (5 days) is expected to increase the accuracy of leaf CC estimation. To date, algorithms to estimate CC based on Sentinel 2 simulated spectral bands are being revised, created, and validated in crops across Europe, showing promising results [93–95]. Therefore, there is much scope for the application of these algorithms to estimate CC in mangrove forests once Sentinel 2 is operational.

5. Conclusions

The results presented in this work add to our understanding of the relationship between vegetation indices and the biochemical composition of mangrove by showing which multispectral and hyperspectral indices best explain the variation in chlorophyll concentration at the leaf and canopy level. We tested the ability of broad band and hyperspectral VIs to predict mangrove CC at different scales. At leaf level indices with spectral bands around the red edge (705–753 nm), Vogelmann indices and the MTCI were the most sensitive to mangrove leaf CC ($R^2 > 0.5$). A key finding was that at ESU level, the best performing Landsat 8 VI was NDVI green, which explained 80% of the variation in CC. The linear model describing the relationship between CC and NDVI green was used to map the spatiotemporal variability of CC in the mangrove landscape. The study demonstrated that the multispectral, medium-resolution Landsat 8 can be used to quantify CC in mangrove forests where ground networks and other possible tools cannot be applied and the use of mapping techniques based on satellite data is absolutely necessary. A practical application of this result is that future efforts to estimate CC in mangrove forests using multispectral remote sensing should consider the use of Landsat 8 NDVI green. The findings also corroborated the utility of the red edge spectral bands to predict mangrove CC at leaf and ESU level. This has implications for the improvement of mangrove monitoring using upcoming technology such as Sentinel 2, which will include two spectral bands around the red edge position. This spectral band arrangement will allow for the computation of VIs highly correlated with CC tested in this work at finer spatial and temporal resolution. It is recommended that future research should focus on testing existing and newly developed algorithms to estimate CC in mangrove forests using the new generation of satellites that outperform the capabilities of current sensors.

Acknowledgments

The authors would like to thank CONACyT for the scholarship provided to Julio Pastor-Guzman to pursue postgraduate studies. We are grateful to A. MacArthur and the Natural Environment Research

Council Field Spectroscopy Facility (NERC FSF) for the loan of the field spectrometer and to NASA for providing Landsat 8 data. Special acknowledgement is due to Israel Medina, Fernando Mex, and Genaro Cob for their support during fieldwork. The research grant SEP-CONACyT No. 153599 provided funding to Rodofo Rioja-Nieto for this research. Finally, the authors thank the three anonymous reviewers for the valuable comments that improved the original manuscript.

Author Contributions

Julio Pastor-Guzman, Peter M. Atkinson, Jadunandan Dash, and Rodofo Rioja-Nieto conceived and designed the experiment; Julio Pastor-Guzman and Rodofo Rioja-Nieto performed the fieldwork data collection; Julio Pastor-Guzman analyzed the data. All authors contributed to the final paper.

Conflicts of Interest

The authors declare no conflict of interest.

References

1. Giri, C.; Ochieng, E.; Tieszen, L.L.; Zhu, Z.; Singh, A.; Loveland, T.; Masek, J.; Duke, N. Status and distribution of mangrove forests of the world using earth observation satellite data: Status and distributions of global mangroves. *Glob. Ecol. Biogeogr.* **2011**, *20*, 154–159.
2. Ewel, K.C.; Twilley, R.R.; Ong, J.E. Different kinds of mangrove forests provide different goods and services. *Glob. Ecol. Biogeogr. Lett.* **1998**, *7*, 83–94.
3. Aburto-Oropeza, O.; Ezcurra, E.; Danemann, G.; Valdez, V.; Murray, J.; Sala, E. Mangroves in the Gulf of California increase fishery yields. *Proc. Natl. Acad. Sci.* **2008**, *105*, 10456–10459.
4. Barbier, E.B.; Hacker, S.D.; Kennedy, C.; Koch, E.W.; Stier, A.C.; Silliman, B.R. The value of estuarine and coastal ecosystem services. *Ecol. Monogr.* **2011**, *81*, 169–193.
5. Vo, Q.T.; Kuenzer, C.; Vo, Q.M.; Moder, F.; Oppelt, N. Review of valuation methods for mangrove ecosystem services. *Ecol. Indic.* **2012**, *23*, 431–446.
6. Matsui, N. Estimated stocks of organic carbon in mangrove roots and sediments in Hinchinbrook Channel, Australia. *Mangroves Salt Marshes* **1998**, *2*, 199–204.
7. Donato, D.C.; Kauffman, J.B.; Murdiyarso, D.; Kurnianto, S.; Stidham, M.; Kanninen, M. Mangroves among the most carbon-rich forests in the tropics. *Nat. Geosci.* **2011**, *4*, 293–297.
8. Liu, H.; Ren, H.; Hui, D.; Wang, W.; Liao, B.; Cao, Q. Carbon stocks and potential carbon storage in the mangrove forests of China. *J. Environ. Manage.* **2014**, *133*, 86–93.
9. Jones, T.G.; Ratsimba, H.R.; Ravaoarinorotsihoarana, L.; Cripps, G.; Bey, A. Ecological variability and carbon stock estimates of mangrove ecosystems in northwestern Madagascar. *Forests* **2014**, *5*, 177–205.
10. Kauffman, J.B.; Heider, C.; Cole, T.G.; Dwire, K.A.; Donato, D.C. Ecosystem carbon stocks of Micronesian mangrove forests. *Wetlands* **2011**, *31*, 343–352.
11. Kauffman, J.B.; Heider, C.; Norfolk, J.; Payton, F. Carbon stocks of intact mangroves and carbon emissions arising from their conversion in the Dominican Republic. *Ecol. Appl.* **2014**, *24*, 518–527.

12. Adame, M.F.; Kauffman, J.B.; Medina, I.; Gamboa, J.N.; Torres, O.; Caamal, J.P.; Reza, M.; Herrera-Silveira, J.A. Carbon stocks of tropical coastal wetlands within the karstic landscape of the Mexican Caribbean. *PLoS ONE* **2013**, *8*, E56569.
13. Barr, J.G.; Engel, V.; Fuentes, J.D.; Zieman, J.C.; O'Halloran, T.L.; Smith, T.J.; Anderson, G.H. Controls on mangrove forest-atmosphere carbon dioxide exchanges in western Everglades National Park. *J. Geophys. Res.* **2010**, *115*, G2.
14. Adame, M.F.; Lovelock, C.E. Carbon and nutrient exchange of mangrove forests with the coastal ocean. *Hydrobiologia* **2011**, *663*, 23–50.
15. Duke, N.C.; Meynecke, J.-O.; Dittmann, S.; Ellison, A.M.; Anger, K.; Berger, U.; Cannicci, S.; Diele, K.; Ewel, K.C.; Field, C.D. A world without mangroves? *Science* **2007**, *317*, 41–42.
16. Valiela, I.; Bowen, J.L.; York, J.K. Mangrove forests: One of the world's threatened major tropical environments. *Bio. Sci.* **2001**, *51*, 807–815.
17. Peñuelas, J.; Filella, I. Visible and near-infrared reflectance techniques for diagnosing plant physiological status. *Trends Plant. Sci.* **1998**, *3*, 151–156.
18. Carter, G.A.; Knapp, A.K. Leaf optical properties in higher plants: Linking spectral characteristics to stress and chlorophyll concentration. *Am. J. Bot.* **2001**, *88*, 677–684.
19. Zhang, C.; Liu, Y.; Kovacs, J.M.; Flores-Verdugo, F.; de Santiago, F.F.; Chen, K. Spectral response to varying levels of leaf pigments collected from a degraded mangrove forest. *J. Appl. Remote Sens.* **2012**, *6*, 063501-1.
20. Zhang, C.; Kovacs, J.; Wachowiak, M.; Flores-Verdugo, F. Relationship between hyperspectral measurements and mangrove leaf nitrogen concentrations. *Remote Sens.* **2013**, *5*, 891–908.
21. Flores-de-Santiago, F.; Kovacs, J.M.; Flores-Verdugo, F. The influence of seasonality in estimating mangrove leaf chlorophyll-a content from hyperspectral data. *Wetl. Ecol. Manag.* **2013**, *21*, 193–207.
22. Flores-de-Santiago, F.; Kovacs, J.; Flores-Verdugo, F. Seasonal changes in leaf chlorophyll a content and morphology in a sub-tropical mangrove forest of the Mexican Pacific. *Mar. Ecol. Prog. Ser.* **2012**, *444*, 57–68.
23. Porra, R.J.; Thompson, W.A.; Kriedemann, P.E. Determination of accurate extinction coefficients and simultaneous equations for assaying chlorophylls a and b extracted with four different solvents: Verification of the concentration of chlorophyll standards by atomic absorption spectroscopy. *Biochim. Biophys. Acta. BBA-Bioenerg.* **1989**, *975*, 384–394.
24. Ritchie, R.J. Consistent sets of spectrophotometric chlorophyll equations for acetone, methanol and ethanol solvents. *Photosynth. Res.* **2006**, *89*, 27–41.
25. Markwell, J.; Osterman, J.C.; Mitchell, J.L. Calibration of the Minolta SPAD-502 leaf chlorophyll meter. *Photosynth. Res.* **1995**, *46*, 467–472.
26. Uddling, J.; Gelang-Alfredsson, J.; Piikki, K.; Pleijel, H. Evaluating the relationship between leaf chlorophyll concentration and SPAD-502 chlorophyll meter readings. *Photosynth. Res.* **2007**, *91*, 37–46.
27. Richardson, A.D.; Duigan, S.P.; Berlyn, G.P. An evaluation of noninvasive methods to estimate foliar chlorophyll content. *New Phytol.* **2002**, *153*, 185–194.

28. Coste, S.; Baraloto, C.; Leroy, C.; Marcon, É.; Renaud, A.; Richardson, A.D.; Roggy, J.-C.; Schimann, H.; Uddling, J.; Hérault, B. Assessing foliar chlorophyll contents with the SPAD-502 chlorophyll meter: A calibration test with thirteen tree species of tropical rainforest in French Guiana. *Ann. For. Sci.* **2010**, *67*, 607.
29. Mielke, M.S.; Schaffer, B.; Li, C. Use of a SPAD meter to estimate chlorophyll content in *Eugenia Uniflora L.* leaves as affected by contrasting light environments and soil flooding. *Photosynthetica* **2010**, *48*, 332–338.
30. Connelly, X.M. The Use of a chlorophyll meter (SPAD-502) for field determinations of red mangrove (*Rhizophora Mangle L.*) leaf chlorophyll amount. *NASA Univ. Res. Cent. Tech. Adv. Educ. Aeronaut. Space Auton. Earth Environ.* **1997**, *1*, 187–190.
31. Biber, P.D. Evaluating a chlorophyll content meter on three coastal wetland plant species. *J. Agric. Food Environ. Sci.* **2007**, *1*, 1–11.
32. Flores-de-Santiago, F.; Kovacs, J.M.; Flores-Verdugo, F. Assessing the utility of a portable pocket Instrument for estimating seasonal mangrove leaf chlorophyll contents. *Bull. Mar. Sci.* **2013**, *89*, 621–633.
33. Goel, N.S.; Thompson, R.L. A snapshot of canopy reflectance models and a universal model for the radiation regime. *Remote Sens. Rev.* **2000**, *18*, 197–225.
34. Houborg, R.; Soegaard, H.; Boegh, E. Combining vegetation index and model inversion methods for the extraction of key vegetation biophysical parameters using Terra and Aqua MODIS reflectance data. *Remote Sens. Environ.* **2007**, *106*, 39–58.
35. Houborg, R.; Anderson, M.C. Utility of an image-based canopy reflectance modeling tool for remote estimation of LAI and leaf chlorophyll content at regional scales. *J. Appl. Remote Sens.* **2009**, *3*, 29.
36. Combal, B.; Baret, F.; Weiss, M.; Trubuil, A.; Mace, D.; Pragnere, A.; Myneni, R.; Knyazikhin, Y.; Wang, L. Retrieval of canopy biophysical variables from bidirectional reflectance: Using prior information to solve the ill-posed inverse problem. *Remote Sens. Environ.* **2002**, *84*, 1–15.
37. Jacquemoud, S.; Baret, F.; Andrieu, B.; Danson, F.M.; Jaggard, K. Extraction of vegetation biophysical parameters by inversion of the PROSPECT + SAIL models on sugar beet canopy reflectance data. Application to TM and AVIRIS sensors. *Remote Sens. Environ.* **1995**, *52*, 163–172.
38. Jacquemoud, S.; Verhoef, W.; Baret, F.; Bacour, C.; Zarco-Tejada, P.J.; Asner, G.P.; François, C.; Ustin, S.L. PROSPECT+SAIL models: A review of use for vegetation characterization. *Remote Sens. Environ.* **2009**, *113*, S56–S66.
39. Darvishzadeh, R.; Matkan, A.A.; Ahangar, A.D. Inversion of a radiative transfer model for estimation of rice canopy chlorophyll content using a lookup-table approach. *IEEE J. Sel. Top. Appl. Earth Obs. Remote Sens.* **2012**, *5*, 1222–1230.
40. Dash, J.; Curran, P.J. The MERIS terrestrial chlorophyll index. *Int. J. Remote Sens.* **2004**, *25*, 5403–5413.
41. Gitelson, A.A.; Merzlyak, M.N. Relationships between leaf chlorophyll content and spectral reflectance and algorithms for non-destructive chlorophyll assessment in higher plant leaves. *J. Plant. Physiol.* **2003**, *160*, 271–282.
42. Atzberger, C. Object-based retrieval of biophysical canopy variables using artificial neural nets and radiative transfer models. *Remote Sens. Environ.* **2004**, *93*, 53–67.

43. Blackburn, G.A. Hyperspectral remote sensing of plant pigments. *J. Exp. Bot.* **2007**, *58*, 855–867.
44. Gitelson, A.A. Remote estimation of canopy chlorophyll content in crops. *Geophys. Res. Lett.* **2005**, *32*, doi:10.1029/2005GL022688.
45. Sims, D.A.; Gamon, J.A. Relationships between leaf pigment content and spectral reflectance across a wide range of species, leaf structures and developmental stages. *Remote Sens. Environ.* **2002**, *81*, 337–354.
46. Dash, J.; Curran, P.J. Evaluation of the MERIS terrestrial chlorophyll index (MTCI). *Adv. Space Res.* **2007**, *39*, 100–104.
47. Croft, H.; Chen, J.M.; Zhang, Y.; Simic, A. Modelling leaf chlorophyll content in broadleaf and needle leaf canopies from ground, CASI, Landsat TM 5 and MERIS reflectance data. *Remote Sens. Environ.* **2013**, *133*, 128–140.
48. Croft, H.; Chen, J.M.; Zhang, Y. The applicability of empirical vegetation indices for determining leaf chlorophyll content over different leaf and canopy structures. *Ecol. Complex.* **2014**, *17*, 119–130.
49. Roger O.; Celene E.; Cecilia C.; Carlos, G. Atlas Escenarios de cambio climático en la Península de Yucatán. Available online: http://www.ccpy.webmerida.com.mx/agenda-regional/escenarios-cambio-climatico/atlas/ (accessed on 15 January 2015).
50. Herrera-Silveira, J.A. Overview and characterization of the hydrology and primary producer communities of selected coastal lagoons of Yucatán, México. *Aquat. Ecosyst. Health Manag*. **1999**, *1*, 353–372.
51. Pope, K.O.; Rejmankova, E.; Paris, J.F.; Woodruff, R. Detecting seasonal flooding cycles in marshes of the Yucatan Peninsula with SIR-C polarimetric radar imagery. *Remote Sens. Environ.* **1997**, *59*, 157–166.
52. Lugo, A.E.; Snedaker, S.C. The ecology of mangroves. *Annu. Rev. Ecol. Syst.* **1974**, *1974*, 39–64.
53. Batllori-Sampedro, E.; Febles-Patrón, J.L.; Diaz-Sosa, J. Landscape change in Yucatan's northwest coastal wetlands (1948–1991). *Hum. Ecol. Rev.* **1999**, *6*, 8–20.
54. Acosta Lugo, E.; Alonso Parra, D.; Andrade Hernández, M.; Castillo Tzab, D.; Chablé Santos, J.; Durán García, R.; Espadas Marnrique, C.; Fernández Stochanlova, I.; Fraga Berdugo, J.; Galicia, E.; *et al*. *Plan. de Conservación de la Eco-Región: Petenes.-Celestún-Palmar*; Pronatura Península de Yucatán, Universidad de Yucatán, Centro de Investigaciones y de Estudios Avanzados Universidad Autónoma de Campeche, Centro EPOMEX: Campeche, Mexico, 2010.
55. Naidoo, G. Factors contributing to dwarfing in the mangrove avicennia marina. *Ann. Bot.* **2006**, *97*, 1095–1101.
56. Sternberg, L. da S.L.; Teh, S.Y.; Ewe, S.M.L.; Miralles-Wilhelm, F.; DeAngelis, D.L. Competition between hardwood hammocks and mangroves. *Ecosystems* **2007**, *10*, 648–660.
57. Blasco, F.; Gauquelin, T.; Rasolofoharinoro, M.; Denis, J.; Aizpuru, M.; Caldairou, V. Recent advances in mangrove studies using remote sensing data. *Mar. Freshw. Res.* **1998**, *49*, 287–296.
58. Buckley, T.N.; Cescatti, A.; Farquhar, G.D. What does optimization theory actually predict about crown profiles of photosynthetic capacity when models incorporate greater realism? *Plant. Cell. Environ.* **2013**, *36*, 1547–1563.
59. Cerovic, Z.G.; Masdoumier, G.; Ghozlen, N.B.; Latouche, G. A new optical leaf-clip meter for simultaneous non-destructive assessment of leaf chlorophyll and epidermal flavonoids. *Physiol. Plant.* **2012**, *146*, 251–260.

60. Marenco, R.A.; Antezana-Vera, S.A.; Nascimento, H.C.S. Relationship between specific leaf area, leaf thickness, leaf water content and SPAD-502 readings in six Amazonian tree species. *Photosynthetica* **2009**, *47*, 184–190.
61. Jordan, C. F. Derivation of Leaf-Area Index from Quality of Light on the Forest Floor. *Ecology* **1969**, 50, 663–666.
62. Gitelson, A.; Merzlyak, M. N. Quantitative estimation of chlorophyll-a using reflectance spectra - experiments with autumn chestnut and maple leaves. *J. Photochem. Photobiol. B-Biol*. **1994**, 22, 247–252.
63. Rouse, J. W., Jr.; Haas, R. H.; Schell, J. A.; Deering, D. W. Monitoring Vegetation Systems in the Great Plains with Erts. *NASA Spec. Publ*. **1974**, 351, 309.
64. Vogelmann, J. E.; Rock, B. N.; Moss, D. M. Red edge spectral measurements from sugar maple leaves. *Int. J. Remote Sens*. **1993**, 14, 1563–1575.
65. Zarco-Tejada, P. J.; Miller, J. R.; Noland, T. L.; Mohammed, G. H.; Sampson, P. H. Scaling-up and model inversion methods with narrowband optical indices for chlorophyll content estimation in closed forest canopies with hyperspectral data. *IEEE Trans. Geosci. Remote Sens*. **2001**, 39, 1491–1507.
66. Gamon, J. A.; Peñuelas, J.; Field, C. B. A narrow-waveband spectral index that tracks diurnal changes in photosynthetic efficiency. *Remote Sens. Environ*. **1992**, 41, 35–44.
67. Haboudane, D.; Miller, J. R.; Tremblay, N.; Zarco-Tejada, P. J.; Dextraze, L. Integrated narrow-band vegetation indices for prediction of crop chlorophyll content for application to precision agriculture. *Remote Sens. Environ*. **2002**, 81, 416–426.
68. Wu, C.; Niu, Z.; Tang, Q.; Huang, W. Estimating chlorophyll content from hyperspectral vegetation indices: Modeling and validation. *Agric. For. Meteorol.* **2008**, *148*, 1230–1241.
69. Gitelson, A.A.; Kaufman, Y.J.; Merzlyak, M.N. Use of a green channel in remote sensing of global vegetation from EOS-MODIS. *Remote Sens. Environ.* **1996**, *58*, 289–298.
70. Liu, H. Q.; Huete, A. A feedback based modification of the NDVI to minimize canopy background and atmospheric noise. *IEEE Trans. Geosci. Remote Sens*. **1995**, 33, 457–465.
71. Jiang, Z.; Huete, A. R.; Didan, K.; Miura, T. Development of a two-band enhanced vegetation index without a blue band. *Remote Sens. Environ*. **2008**, 112, 3833–3845.
72. Gitelson, A. A. Wide Dynamic Range Vegetation Index for Remote Quantification of Biophysical Characteristics of Vegetation. *J. Plant Physiol*. **2004**, 161, 165–173.
73. Gitelson, A. A.; Peng, Y.; Masek, J. G.; Rundquist, D. C.; Verma, S.; Suyker, A.; Baker, J. M.; Hatfield, J. L.; Meyers, T. Remote estimation of crop gross primary production with Landsat data. *Remote Sens. Environ*. **2012**, 121, 404–414.
74. Mapa de uso del suelo y vegetación de la zona costera asociada a los manglares Available online: http://www.conabio.gob.mx/informacion/gis/ (accessed on 15 January 2015).
75. Lachenbruch, P.; Mickey, R. Estimation of error rates in discriminant analysis. *Thechnometrics* **1968**, *10*, 1–11.
76. R Development Core Team *R: A Language and Environment for Statistical Computing*; R Foundation for Statistical Computing: Vienna, Austria, 2012.
77. Slaton, M.R.; Hunt, E.R.; Smith, W.K. Estimating near-infrared leaf reflectance from leaf structural characteristics. *Am. J. Bot.* **2001**, *88*, 278–284.

78. Rebelo-Mochel, F.; Ponzoni, F.J. Spectral characterization of mangrove leaves in the Brazilian Amazonian Coast: Turiaçu Bay, Maranhão State. *An. Acad. Bras. Ciênc.* **2007**, *79*, 683–692.
79. Lima, C.S.; Boeger, M.R.T.; Larcher-de Carvalho, L.; Pelozo, A.; Soffiatti, P. Sclerophylly in mangrove tree species from South Brazil. *Rev. Mex. Biodivers.* **2013**, *84*, 1159–1166.
80. Xiao, Y.; Jie, Z.; Wang, M.; Lin, G.; Wang, W. Leaf and stem anatomical responses to periodical waterlogging in simulated tidal floods in mangrove avicennia marina seedlings. *Aquat. Bot.* **2009**, *91*, 231–237.
81. Camilleri, J.C.; Ribi, G. Leaf thickness of mangroves (*rhizophora mangle*) growing in different salinities. *Biotropica* **1983**, *15*, 139–141.
82. Sobrado, M.A. Leaf characteristics and gas exchange of the mangrove *laguncularia racemosa* as affected by salinity. *Photosynthetica* **2005**, *43*, 217–221.
83. Parida, A.K.; Das, A.B.; Mittra, B. Effects of salt on growth, ion accumulation, photosynthesis and leaf anatomy of the mangrove, *bruguiera parviflora*. *Trees* **2004**, *18*, 167–174.
84. Gitelson, A.A.; Merzlyak, M.N. Remote estimation of chlorophyll content in higher plant leaves. *Int. J. Remote Sens.* **1997**, *18*, 2691–2697.
85. Gitelson, A.A.; Viña, A.; Verma, S.B.; Rundquist, D.C.; Arkebauer, T.J.; Keydan, G.; Leavitt, B.; Ciganda, V.; Burba, G.G.; Suyker, A.E. Relationship between gross primary production and chlorophyll content in crops: Implications for the synoptic monitoring of vegetation productivity. *J. Geophys. Res.* **2006**, *111*, D8.
86. Rossini, M.; Migliavacca, M.; Galvagno, M.; Meroni, M.; Cogliati, S.; Cremonese, E.; Fava, F.; Gitelson, A.; Julitta, T.; di Cella, U.M.; *et al*. Remote estimation of grassland gross primary production during extreme meteorological seasons. *Int. J. Appl. Earth Obs. Geoinform.* **2014**, *29*, 1–10.
87. Green, E.P.; Edwards, A.J. *Remote Sensing Handbook for Tropical Coastal Management*; UNESCO Publisher: Paris, France, 2000.
88. Roberts, D.A.; Ustin, S.L.; Ogunjemiyo, S.; Greenberg, J.; Dobrowski, S.Z.; Chen, J.; Hinckley, T.M. Spectral and structural measures of northwest forest vegetation at leaf to landscape scales. *Ecosystems* **2004**, *7*, 545–562.
89. Díaz, B.M.; Blackburn, G.A. Remote sensing of mangrove biophysical properties: Evidence from a laboratory simulation of the possible effects of background variation on spectral vegetation indices. *Int. J. Remote Sens.* **2003**, *24*, 53–73.
90. Wagner, F.; Rossi, V.; Stahl, C.; Bonal, D.; Hérault, B. Asynchronism in leaf and wood production in tropical forests: A study combining satellite and ground-based measurements. *Biogeosciences* **2013**, *10*, 7307–7321.
91. Zaldivar-Jimenez, A.; Herrera-Silveira, J.; Coronado-Molina, C.; Alonzo-Parra, D. Structure and productivity of Ria Celestun Biosphere Reserve mangrove forest, Yucatan, Mexico. *Wood For.* **2004**, *10*, 25–35.
92. Drusch, M.; Del Bello, U.; Carlier, S.; Colin, O.; Fernandez, V.; Gascon, F.; Hoersch, B.; Isola, C.; Laberinti, P.; Martimort, P.; *et al*. Sentinel-2: ESA's optical high-resolution mission for GMES operational services. *Remote Sens. Environ.* **2012**, *120*, 25–36.
93. Delegido, J.; Vergara, C.; Verrelst, J.; Gandía, S.; Moreno, J. Remote estimation of crop chlorophyll content by means of high-spectral-resolution reflectance techniques. *Agron. J.* **2011**, *103*, 1834–1842.

94. Delegido, J.; Verrelst, J.; Alonso, L.; Moreno, J. Evaluation of Sentinel-2 red-edge bands for empirical estimation of green LAI and chlorophyll content. *Sensors* **2011**, *11*, 7063–7081.
95. Frampton, W.J.; Dash, J.; Watmough, G.; Milton, E.J. Evaluating the capabilities of Sentinel-2 for quantitative estimation of biophysical variables in vegetation. *ISPRS J. Photogramm. Remote Sens.* **2013**, *82*, 83–92.